Cavitation bubble dynamics in a shear-thickening fluid

Guillaume T. Bokman* and Outi Supponen
Insitute of Fluid Dynamics,
Department of Mechanical and Process Engineering,
ETH Zurich,
Sonneggstrasse 3,
8092 Zurich, Switzerland

Simo A. Mäkiharju†
University of California, Berkeley
6119 Etcheverry Hall,
Berkeley, CA 94720, USA
(Dated: April 12, 2022)

Cavitation has been extensively studied in Newtonian fluids, and to a lesser yet significant degree in shear-thinning fluids. However, cavitation has not been previously investigated in shear-thickening fluids, of which a water-cornstarch suspension is perhaps the best-known example. An interesting property of such fluids is that, when subjected to an increase in strain rate, their viscosity increases until they exhibit solid-like behavior and can even fracture. As cavitation bubbles are capable of generating extreme strain rates, they could be affected by shear-thickening fluid behaviour. As visual access is limited by opaque or non-index-matched particles present in such fluids, an experimental study of nominally cylindrical spark-induced cavitation bubbles is conducted in a 2-mm gap between two parallel flat and transparent plates, which allows visualization of the bubbles as they contact the boundary. They are theoretically studied through the cylindrical Keller-Miksis equation adapted to a shear-thickening fluid using a Cross model. For volume fractions starting from $\phi = 0.44$, the limit between continuous and discontinuous shear thickening regime, cavitation bubbles deform increasingly until they are replaced by cavitation-induced fracture between $\phi = 0.46$ and $\phi = 0.52$. Fracture propagation speeds were found to be in the same range as fracture speeds previously reported for pressure-driven cavity expansion, albeit for estimated initial pressures that are now orders of magnitude higher.

I. INTRODUCTION

The properties of shear-thickening fluids make them suitable for a variety of applications involving strong dynamic events, including personnel protection. There has been considerable research in the field of liquid body armors, where shear-thickening silica suspensions are generally combined with Kevlar [1–3] to improve the ballistic penetration resistance of the fabric. In general, when such a fluid comes under stress, the suspended particles interact, modifying the fluid's properties. Although not yet fully understood, the resulting behavior can be classified into three different regimes of interest depending on the concentration of solid particles present in the suspension and stress applied to it: continuous shear thickening (CST), discontinuous shear thickening (DST) and shear jamming (SJ) [4]. The increase in fluid viscosity with increasing strain rate is continuous in the case of CST and almost discontinuous in the case of DST. SJ is the most extreme region where the fluid becomes solid-like and is prone to undergoing fracture.

In the event of a small projectile entering a viscoelastic or shear-thickening fluid, it has been shown that its speed after impact is reduced in comparison to water, and that the projectile may cause the fluid to vaporize along its path [5]. That is, cavitation may occur due to a sudden decrease in pressure or by a sudden increase in temperature. Cavitation has been extensively studied in Newtonian fluids [6] and has also received a fair amount of attention in non-Newtonian shear-thinning fluids such as blood [7] and shear-thinning polymer solutions [8, 9]. In developing cavitation-induced jet printing, cavitation in viscoplastic fluids [10], as well as viscoelastic films [11] have also been studied. Research in viscoelastic fluids [12–15] and solid shells [16–18] have shown that the general equations of motion for a spherical cavitation bubble can be modified from a Newtonian fluid to non-Newtonian by constitutive models, such as the Williamson, Kelvin–Voigt, linear Maxwell or 4-constant Oldroyd models. Cavitation rheology is, in fact, an emerging field that has been used for investigating the material properties of biological tissues [19] and soft materials such as polyacrylamide [20] and poly(vinyl alcohol) hydrogels [21], exploiting cavitation to probe strain rates not attainable by existing rheometers. In these studies, sparks [e.g., 22] or lasers [e.g., 23] are commonly used to generate the cavitation bubbles. However, no study on cavitation in shear-thickening fluids has yet been reported.

Possibly the best-known shear-thickening fluid is a cornstarch particle suspension in water, commonly re-

* Visiting student at University of California, Berkeley, USA
† Spokesperson: makiharju@berkeley.edu

ferred to as Oobleck. It has been studied extensively [24–27] and is composed of readily available materials. As this particular candidate, like most particle suspensions, is optically opaque, a narrow nominally 2D geometry, inspired by Hele-Shaw cells, can be used to enable visualization of the movement of the fluid interface. Recently, continuous and discontinuous shear-thickening as well as fracture due to injection of pressurized gas into a shear-thickening fluid has been investigated in Hele-Shaw cells as a function of a particle suspension's volume fraction in cornstarch [24] and glass beads [28] suspensions, where both have investigated the Saffman-Taylor instability in particle suspensions, capable of producing fracture at high volume fraction.

This work presents experimental and theoretical investigations of cavitation bubbles in a shear–thickening cornstarch particle suspension in water with varying solids volume fraction. The effects of the high strain rates produced by cavitation on the resulting dynamics are assessed, and the different shear-thickening regimes, as well as fracture, are expected to be encountered, depending on the particle volume fraction. The observed bubble dynamics are contrasted to those one would observe in a Newtonian fluid to evaluate the effects of shear-dependent viscosity.

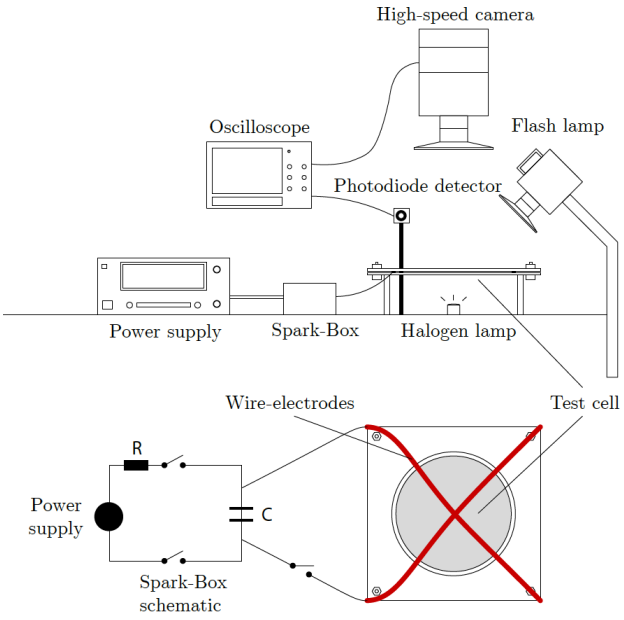

FIG. 1. Side and top view schematic of the experimental setup. The shaded circle is the test cell with height $H = 2$ mm and radius $R_{\text{cell}} = 100$ mm, where spark-induced nominally cylindrical cavitation bubbles are studied. Cavitation occurs at the center of the cell where the wire-electrodes (red lines of exaggerated thickness) cross. The RC electrical circuit includes switches, a DC power supply, resistor with resistance R, and capacitor of capacitance C.

II. METHODS

A. Experimental setup

In order to visualize cavitation in an opaque particle suspension, an experimental setup capable of producing nominally cylindrical cavitation bubbles in a narrow gap between two parallel plates is utilized. Figure 1 shows the overall experimental setup and the electrical schematic used to generate the spark in the center of the fluid-filled gap. The spark deposits a large amount of energy in a small region resulting in vaporization of the liquid. The generated bubble contains vapor and traces of non-condensable gases, and expands until it reaches a maximum size. This maximum size depends on the fluid properties and the deposited energy. Upon reaching the maximum radius, a collapse immediately follows due to the pressure difference within the bubble and surrounding fluid, and if sufficient energy remains after collapse, the bubble rebounds to a smaller maximum radius and the cycle repeats itself until excess energy is dissipated [6, 29].

The test cell consists of two flat plates separated by a 3D printed polylactide spacer ring with an inner radius of $R_{\text{cell}} = 100$ mm, outer radius of 110 mm, height of $H = 2$ mm, and nominal dimensional uncertainty of 0.1 mm. The ring also has four 0.25-mm wide and 1-mm deep slits to allow for repeatable positioning of wire-electrodes, which cross at the cell's center and are kept under constant tension to ensure contact. The spacer ring is glued on top of a 300 x 300-mm transparent 4-mm thick Plexiglas plate forming a reservoir to contain the fluid. The test cell is sealed by tightening a second identical Plexiglas plate on top of the ring with bolts and nuts at the four corners. However, during cavitation, small droplets are occasionally observed ejecting out from the wire slits. The cavitation bubble is generated within the incompressible fluid surrounded by the rigid ring. The expansion of the volume due to a 3-mm radius bubble would be accommodated by a mere 0.1% expansion of the volume, which in a perfectly rigid container would results in a 2.2-MPa increase in liquid pressure for a 2.2-GPa water bulk modulus. It is more likely that the gap formed by thin walls expands by $\sim$2 μm in order to accommodate the cavity. This increase in gap being considered small enough, the cell is assumed nominally rigid.

Figure 1 also shows the electrical schematic of an RC circuit, which is similar to that used in a previous study by [22]. The circuit enclosed in a "Spark-Box" consists of an inner loop with a 3-W, 2-kOhm, $\pm$5% resistor, a 3300-μF, 9.7-A, 350-V, $\pm$20% electrolytic capacitor, 22-AWG wires, and an electrical switch to fully separate the capacitor from the 200-V, 2-A, 160-W power supply (Elektro-Automatik). The outer circuit consists of a switch and 14-AWG wires to reduce the resistance, as this affects the discharge time. The heavier wire is connected at the test cell to the 34-AWG copper wires used as wire-electrodes and replaced after each experiment.

The typical voltage at which the capacitor is charged ranges from $V_{DC} = 50$–80 V, which is found to produce cylindrical bubbles of maximum radii within the range $R_{\max} \approx 3$–8 mm. The discharge time constant, τ, can be computed by using the wire resistance $R_{\rm w}$ and capacitor capacitance C, $\tau = R_{\rm w}C \approx 0.62$ ms. Hence it is noted that for the smallest bubbles examined, the amount of time to reach their maximum radius can be shorter than τ, in which case the start of the collapse may be delayed by the spark being still on. Such bubbles are excluded from our analysis.

The cavitation bubbles are imaged from above the test cell via a high-speed camera (Photron Fastcam Nova S12) with a resolution of 160 x 256 pixels at 125 kFPS. A photodiode detector (Thorlabs, DET10A2) with a rise time of 1 ns is connected to an oscilloscope and pointed at the cell center to trigger the high-speed camera upon the spark ignition. When experiments are conducted in water, a broadband halogen fiber optic illuminator (Thorlabs, OSL2), located under the test cell, is used as a backlight to enable bubble shadowgraphy. In opaque cornstarch suspensions, the backlight is replaced by a flash-lamp (Cordin 605) placed above the test cell and used as a frontlight. The image data are analyzed by a Matlab script implementing gamma correction, Otsu edge threshold used for binarization, and Canny edge-detection. The processed results are verified by superimposing the detected edge on the respective video frames. Subsequently, the bubble's nominal radius is extracted by counting the number of pixels contained within the detected edge, and computing the equivalent circular shape of the same area. This procedure is necessary especially at higher solids fractions, where the shape of the bubble is not circular. The overall uncertainty on the computation of the radius is estimated to be two pixels, or 0.22 mm.

The temperature of the fluid is recorded using a thermocouple and found to be $T_\infty = 20 \pm 1°$C. The local atmospheric pressure is given by the nearby Swiss meteorology weather station and amounts to $p_\infty = 1.00 \pm 0.03$ bar. When investigating repeatability, the maximum bubble radius is found to have a standard deviation up to 14% of the mean of 14 tests in water, keeping all factors nominally constant.

B. Fluid characterization

The shear-thickening particle suspensions utilized are composed of cornstarch and deionized water at solids volume fractions ranging from $\phi = 0.00$ to 0.52 ± 0.01. Water and cornstarch densities based on literature are $\rho_{\rm w} = 998$ kg/m^3 and $\rho_{\rm c} = 1600$ kg/m^3, respectively, with cornstarch density verified from measurements and a simple mean field approach of [26]. Samples are manufactured by mixing 250-g packs of bulk Maizena cornstarch with the required amount of deionized water to reach the desired volume fraction. The mean diameter of cornstarch particles, $d_{\rm p} = 9.66 \pm 4.50$ μm is measured by a particle sizer (Beckman Coulter, Multizer 4e).

While the liquid and solid densities are not matched, [30] showed that sedimentation can still be avoided if the cornstarch suspension is stirred properly prior to experiment, and this also ensures homogeneity of the mixture.

Furthermore, the justification to expect homogeneity of a particle suspension in the neighbouring of a collapsing bubble, capable of inducing extreme accelerating flow, can be verified by calculating the particle response time, or Stokes time. It is the timescale for particles to follow the accelerating flow and estimated as $\tau_{\rm p} = d_{\rm p}^2/(3\beta\nu)$, where β is the density ratio between the fluid and particle, $\beta = 3\rho_{\rm w}/(\rho_{\rm w} + 2\rho_{\rm c})$, and ν is the kinematic viscosity of the fluid. The particle response time is estimated to be between 12-94 μs, which is at least an order of magnitude lower than the bubble dynamics, which correspond to an oscillation period of 400-2800 μs in the cases examined.

The assumption of negligible sedimentation is experimentally confirmed by delaying tests for more than a few minutes instead of the actual maximum of 40 seconds from deposition of the continuously stirred fluid into the test cell to spark ignition. In those cases, sedimentation effects can clearly be observed, as water moves faster on the top layer than the particle-laden suspension at the bottom of the test cell, and separation can clearly be seen.

Whether the particles and fluid could segregate due to the acceleration caused by cavitation can also be considered. However, for 20 μm particles, whose sizes are in the same order of magnitude as the ones used in the present study, [31] showed that these should not be significantly accelerated at a different rate than the fluid. Similarly, radial segregation that would lead to the fluid becoming clearer in the immediate boundary of the cavitation bubbles has not been observed in the present study.

It is worth mentioning that, since this research is not focused on the rheological properties of cornstarch suspensions *per se*, a few aspects are neglected to simplify the experiments. The fluid is not degassed nor sonicated, and the cornstarch is not dried prior to mixing to remove ambient humidity. It is, however, accounted for by using the average moisture content of cornstarch [32], $\xi = 0.10 \pm 0.01$. The volume fraction ϕ is corrected accordingly, such as:

$$\phi = \frac{(1-\xi)m_{\rm c}/\rho_{\rm c}}{(1-\xi)m_{\rm c}/\rho_{\rm c} + m_{\rm w}/\rho_{\rm w} + \xi m_{\rm c}/\rho_{\rm w}}(1+\lambda), \qquad (1)$$

where $m_{\rm c}$ is the mass of cornstarch and $m_{\rm w}$ the mass of deionized water. The pore space in cornstarch that can absorb water when fully submerged, λ is also considered, and its value is 0.3 [33]. These approximations are common in the literature [26, 30], and hence adopted in the present study as well.

Figure 2 displays the rheology measurements showing the evolution of the shear viscosity, μ and shear stress, τ, with varying shear rate, $\dot{\gamma}$, for four cornstarch suspensions of different volume fractions. Measurements are

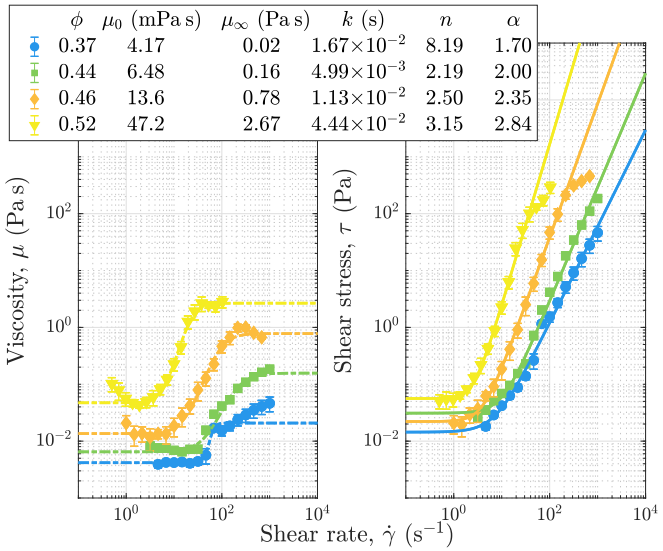

FIG. 2. Measured shear viscosity μ and shear stress τ of cornstarch suspensions of four different volume fractions ϕ as a function of shear rate $\dot{\gamma}$. The dash-dotted lines represent weight-fitted Cross models (with fit parameters given in the legend), characterized by the zero and infinite shear rate viscosity, respectively μ_0 and μ_∞, the relaxation time k and a dimensionless power index n. The solid lines are weight-fitted Power laws, $\tau \propto \dot{\gamma}^\alpha$, fitted to the shear-thickening part of the data and whose exponent value indicate the shear-regime of each mixture. The error bars, hidden by the marker on some points, indicate the standard deviation of the three tests conducted for each suspension.

conducted using an Anton Paar MCR 502 shear rheometer and a 20-mm plate geometry with a 0.8-mm gap. A 19-points shear sweep rheological measurement is conducted with the shear rate as a variable and chosen from a logarithmic profile. All four tested samples show a shear-thickening behaviour over the range of shear rates they were subjected to. After a first shear-thinning phase, they show continuous shear thickening (CST), a continuous increase in fluid viscosity with increasing strain rate, which may be due to the shear-induced formation of hydrodynamic clusters [34]. For high enough shear rates, these hydrodynamic clusters start to locally aggregate, leading to a sudden increase in viscosity. This regime is called discontinuous shear thickening (DST) and is not obvious in Fig. 2. Although the limit between these regimes is not easy to distinguish, by computing α, which is the exponent of the power law $\tau \propto \dot{\gamma}^\alpha$ fitted to the shear stress vs. strain rate displayed in Fig. 2, it is possible to define a limit between these behaviours. If $\alpha \geq 2$, the particle suspension will often be referred as discontinuous [4]. However, this definition can be taken with a grain of salt, especially since there are no clear discontinuous jumps in the viscosity measurements. Nonetheless, since a value of $\alpha = 2.00$ has been found for $\phi = 0.44$ and experiments start showing bubble deformation for these and higher solid's volume fractions, it is assumed that DST is encountered. Note that, when increasing volume fractions, the transition into CST and DST happen for shear rate values which are lower and closer to each other, up to a critical value ϕ_c, where they vanish and the mixture directly undergoes shear jamming (SJ) [25].

The standard deviations of three different tests conducted for each volume fractions in Fig. 2 indicate that the measurements are consistent, and the data compare favorably to literature [24]. Sedimentation is assumed to not play an important role in this case due to the sample being constantly under shear-stress during experiments. Although it is unclear if cornstarch moisture content is accounted for in studies by [25] and [27], their measurements conducted with a different geometry show values in the same order of magnitude, albeit still relatively far from ours. The moisture effects and limitations of the method together with the assumption of negligible sedimentation, might lead to discrepancies when using the measured rheological data to simulate the viscous term in cavitation bubble dynamics equations.

For its simplicity and adequate fit to the data in Fig. 2, the Cross model [35] is chosen to describe the strain rate-dependent viscosity over alternative models such as Sisko, Carreau, and others. However, it should be noted that a few studies with different viscosity measurement techniques also report highly non-Cross behavior showing shear thinning at very low and high shear-rates [25, 36], the latter being expected to be relevant for cavitation bubbles. It has been referred to as an instability and breakdown of local shear-jamming effects, which may originate from the elasticity of particles at very high shear-rates [37]. The parameters of the Cross model are μ_0 and μ_∞, which are respectively the zero and infinite shear viscosities, the relaxation time k, and the power index n. Both viscosities are assumed constant at low and high shear rates, which will impact the modelling, since cavitation bubbles mostly produce extreme strain rates in the order of $10^3 - 10^8$ s^{-1} [20]. The relaxation time represents the characteristic time a material takes to relax once the applied rate of deformation is reduced to zero, and is inversely proportional to the shear rate at which the viscosity reaches μ_∞. The power index represents the slope of the transition from μ_0 to μ_∞ with increasing shear rate $\dot{\gamma}$.

While cavitation bubbles produce extensional strain, only the shear-dependent viscosity is characterized through rheometry measurements. However, the shear viscosity can be transformed into the extensional viscosity μ_e via what has been defined as the Trouton ratio, $\mathrm{Tr} = \mu_e/\mu$ [38]. In the case of a particle suspension under uniaxial flow, it has been shown numerically that the Trouton ratio for particle suspensions keeps a constant value of $\mathrm{Tr} = 3$, as for a uniaxial flow in a Newtonian fluid, until the volume fraction approaches the jamming point, beyond which it increases for frictional particles [39]. This is however still considered an "unexplored area" according to [40], with few experimental studies on extensional rheometry in particle suspensions [41]. Fur-

thermore, if a range of strain rates is investigated, it is far from the ones generated by cylindrical cavitation [42]. In the present study, a constant value is therefore assumed up to solids fraction of $\phi = 0.44$, which is the limit between the CST and DST regimes. The same value for Tr is assumed to also hold for $\phi = 0.46$, although it might be underestimated given the proximity to the jamming point. The radial component of the deviatoric stress tensor τ_{rr} can be adapted from a Newtonian fluid to a shear-thickening one by replacing the constant viscosity by a Cross model's strain-dependent viscosity:

$$\tau_{rr} = 2\mu_e\dot{\epsilon}_{rr} = 6\mu_\infty\dot{\epsilon}_{rr} + \frac{6(\mu_0 - \mu_\infty)}{1 + (k\dot{\epsilon}_{rr})^n}\dot{\epsilon}_{rr}, \tag{2}$$

This is only dependent on the radial component of the strain-rate tensor $\dot{\epsilon}$, and the conversion from shear to extensional viscosity is accounted for by multiplying the Cross model by Tr = 3.

The speed of sound, density, surface tension and viscous stress tensor are considered for the water and cornstarch suspension at each volume fractions. The density is simply computed, and the speed of sound in non-density matched cornstarch suspensions in water is extrapolated to be between 1660 and 1757 m/s for volume fractions of respectively 0.37 and 0.46, based on the data of [26]. The surface tension has also been reported to be slightly lower than that of water for cornstarch suspensions of mass fraction of $w = 0.30$ [43]. However, as it is of the same order of magnitude and its impact on bubble dynamics is negligible due to the dominating inertial effects, the surface tension of water at 20°C is used, i.e., $\sigma = 73$ mN/m.

III. THEORY

Fortuitously, cylindrical cavitation in a Newtonian fluid has previously been studied, laying a solid basis for the theoretical aspects of this research. Previous studies of cavitation bubbles in microfluidic gaps have applied the incompressible cylindrical Rayleigh equation and the accompanying fitted parameter, R_∞, symbolizing the distance from the bubble center to the point at which the fluid does not feel the bubble's motion anymore due to the compressibility of the fluid [44–46]. A past study of collapsing vortex rings yielded the Rayleigh collapse time adapted to a cylindrical geometry [47], which reads:

$$\begin{aligned} T_\mathrm{c} &= 0.915R_0\Big(\frac{\rho_\infty}{p_\infty - p_\mathrm{v}(T_\infty)}\Big)^{\frac{1}{2}}\log\Big(\frac{R_\infty}{R_0}\Big)^{\frac{1}{2}} \\ &= T_{\mathrm{c,spherical}}\log\Big(\frac{R_\infty}{R_0}\Big)^{\frac{1}{2}}, \end{aligned} \tag{3}$$

where R_0 is the bubble's maximum radius before the beginning of the collapse, ρ_∞ and p_∞ are the homogeneous density and pressure of the medium, respectively, $p_\mathrm{v}(T_\infty)$ is the temperature-dependent vapor pressure in the medium and $T_{\mathrm{c,spherical}}$ is the Rayleigh collapse time defined for spherical bubbles [48].

The effects of viscosity alone in a continuous shear-thickening fluid can be simulated and compared to a Newtonian viscous fluid as long as the volume fractions of a particle suspension is sufficiently far from the shear jamming point, where fracture is expected to occur. The Gilmore equation [49] in cylindrical coordinates, simplified into the Keller-Miksis equation [50] is used, as it accounts for compressibility and can be adapted for a shear-thickening fluid. This equation is considered more appropriate than the simple Rayleigh-Plesset [51] equation, as it accounts for the change in speed of sound in cornstarch suspensions with regards to water. However, its accuracy has been reported to be inferior to that of the spherical form due to the cylindrical wave equation assumption for compressibility [52]. The cylindrical Keller-Miksis equation reads:

$$\begin{aligned} &\Big(1 - \frac{\dot{R}}{c_\infty}\Big)R\ddot{R} + \Big(1 - \frac{\dot{R}}{3c_\infty}\Big)\frac{3\dot{R}^2}{4} \\ &= \Big(1 + \frac{\dot{R}}{c_\infty}\Big)\frac{H}{2} + \Big(1 - \frac{\dot{R}}{c_\infty}\Big)\frac{R}{c_\infty}\dot{H}, \end{aligned} \tag{4}$$

where R, $\dot{R}$ and $\ddot{R}$ are the radius, radial velocity and radial acceleration of the bubble interface. The speed of sound c_∞ and density ρ_∞ of the fluid are taken as constants. Here, H and $\dot{H}$ are the enthalpy and first time derivative of the enthalpy of the fluid at the bubble wall, respectively. Enthalpy H is given by:

$$\begin{aligned} H = \frac{p_\mathrm{B}(t) - p_\infty}{\rho_\infty} = \\ \frac{1}{\rho_\infty}\left(p_\mathrm{v}(T_\infty) + p_{\mathrm{g},0}\Big(\frac{R_0}{R}\Big)^{2\kappa} - \frac{\sigma}{R} - p_\infty\right) \\ + \frac{3}{2\rho_\infty}\int_R^\infty \frac{\tau_{rr}}{r}\,dr \end{aligned} \tag{5}$$

The enthalpy consists of the time-dependent pressure at the boundary of the bubble, $p_\mathrm{B}(t)$, and the ambient pressure of the fluid far from the bubble, p_∞. More precisely, the boundary term can be decomposed into a vapor pressure term $p_\mathrm{v}(T_\infty)$, which is taken to be a constant computed from the nominal temperature of the fluid using the Buck equation, the partial pressure of the non-condensable gas $p_{\mathrm{g},0}$ at a reference radius R_0, the polytropic index of the vapor phase κ, and surface tension σ. Note that the viscous term is still in the integral form with respect to the radial component of the cylindrical coordinate system, r.

IV. RESULTS

A. Simulations

Figure 3 shows the temporal evolution of the normalized bubble radius and the absolute strain rate com-

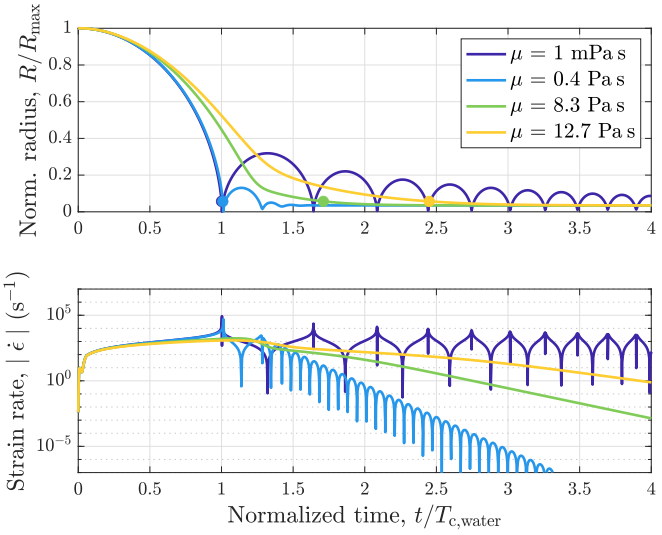

FIG. 3. Normalized radius-time curves (top) of cylindrical bubbles simulated using the Keller-Miksis equation [Eq. (4)] for Newtonian fluids of different shear viscosities, μ, and their corresponding strain-rate-time curves (bottom). The markers show the collapse times according to the chosen definition

puted by numerically solving the Newtonian Keller-Miksis equation. The constant shear viscosity, noted μ for a Newtonian model, is varied to determine its effect on the bubble dynamics. Note that the viscosity is always referred to in terms of shear viscosity to ease comparison to rheometry measurements, but it is the strain viscosity which is considered during theoretical simulations. In order to initially only asses the impact of the viscosity on the bubble dynamics, all constants are selected for water at $T = 20°\text{C}$. The initial conditions for all simulations are $R_{\max} = 5$ mm, which is the typical size obtained during experiments, $\dot{R} = 0$ m/s and $p_{g,0} = 13$ Pa. The estimated value for the initial partial pressure of the non-condensable gas is obtained by numerically fitting the Keller-Miksis equation to the first rebound of experimentally observed bubbles in water having a maximum radius close to $R_{\max} = 5$ mm. This value is assumed to be similar in the cornstarch suspensions in which the experiments are conducted in a similar fashion to those in water, but where the rebounds cannot be visualized. Finally, the time is normalized by the collapse time, T_c, of a simulated 5-mm bubble in water. The simulations, where the equations are solved utilizing an explicit Runge-Kutta formula (ode45 in Matlab), show that for an increase in shear viscosity, the collapse time increases as well, which is in accordance with previous literature and experimental work [e.g., 53, 54]. In other words, an increasing viscosity results in a decrease of the collapse speed and in the dampening of the rebounds until the collapse gets replaced by a monotonically decreasing curve that asymptotically tends toward the equilibrium radius of the bubble. The equilibrium radius can be computed by solving the steady state case of Eq. (5) for R: $(p_v(T_\infty) + p_{g,0}\left(\frac{R_0}{R}\right)^{2\kappa} - \frac{\sigma}{R} - p_\infty)$, which yields $R/R_{\max} = 0.035$ for the simulations of Fig. 3. The critical value $\mu = 3.8$ Pa s for which damped rebounds transition to an asymptotic collapse also depends on these initial conditions. At that moment, the absolute value of the strain rate shows an absolute maximum value not exceeding 10^4 s^{-1}, while for lower viscosity the strain rates reach up to 10^5 s^{-1}. However, these simulated values depend on $R_{\max}$. It is worth noting that for $\mu = 0.4$ Pa s, the integration results in an oscillating strain rate even after the bubble has reached its equilibrium radius, meaning that the simulation is simply integrating around it.

The round markers in Fig. 3 depict the instants chosen in this study as the collapse times based on the arbitrary criteria that bubble has collapsed to within 0.11 mm from the equilibrium radius. Such a definition is needed particularly in the case of an asymptotic collapse, to avoid having non-explicit collapse times. The chosen limit corresponds to the size of a single pixel in our experimental images, below which the image analysis script would not be able to assess variations in the bubble radius evolution. Now that the range of typical strain rates in a Newtonian fluid have been identified, the bubble collapse time one could expect in a shear-thickening fluid is explored through a parameter study. Figure 4 displays contours of the simulated collapse times, according to our previous definition, by numerically solving the Keller-Miksis equation. The viscous term is expressed through the Cross model, and the effects of μ_∞, k and n from Eq. (2) are examined. The zero shear viscosity μ_0, density ρ_∞, speed of sound c_∞, surface tension σ, the isentropic coefficient κ and partial pressure of the vapor phase $p_v(T_\infty)$ are all

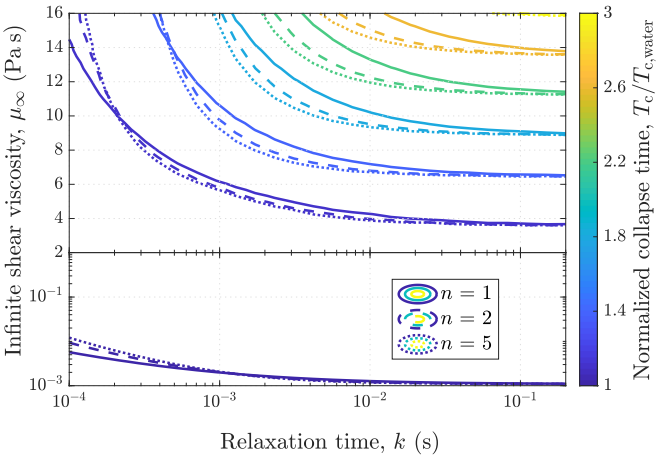

FIG. 4. Contours of the collapse time extracted by numerically solving the Keller-Miksis equation [Eq. (4)] for non-Newtonian fluids as a function of the Cross model [Eq. (2)] parameters: the infinite shear viscosity μ_∞, the relaxation time k and the power index n. The collapse time is normalized to that of a bubble in water, $T_{c,\text{water}}$. All other constants are taken for water at $T_\infty = 20°\text{C}$.

set to the value of water and water vapor at $T_\infty = 20°C$.

The results indicate that for the typical strain rates encountered in Fig. 3, a higher μ_∞, which translates into a higher difference between the zero and infinite shear viscosities, yields a higher collapse time. Similar results have also been found in numerical research on general non-Newtonian fluids such as polymer melts using a power-law model instead of a Cross model [54, 55]. For high relaxation times, k, the fluid finds itself within the μ_∞-regime most of the time, as the shear rates required to reach μ_∞ correspond to the ones expected from any cavitation events, and can thus be compared to a viscous Newtonian fluid with a constant viscosity of μ_∞. The simulated collapse times are also close to that of a cavitation bubble in water for $\mu_\infty < 3 \times 10^{-2}$ Pa s. However, for low relaxation times, this limit gets slightly shifted to higher μ_∞, as the shear rates required to reach μ_∞ in these cases are so high that they are almost never achieved within the simulated conditions.

Contours for three different power indices, $n = 1$, 2, and 5, are also compared. An increase in the exponent beyond $n = 5$ did not yield any appreciable differences. The effect of n on the collapse time appears to become more significant as μ_∞ increases and k decreases, but overall, its role can be considered to be of secondary importance to viscosity as its impact is highly dependent on both parameters.

B. Experiments

1. *Visualizations*

Visualizations of the growth and collapse of cylindrical cavitation bubbles in water and cornstarch suspensions of different volume fractions are shown in Fig. 6. In water, apparent "inner" and "outer" radii of the bubble can be observed, as shown in Fig. 5 and Fig. 6(a). This is caused by the bending of the interface of the cylindrical bubble in the viewing direction. The bubble's interface is bent outwards during expansion and inwards during collapse as displayed in respectively Fig. 5(a) and Fig. 5(c). Fig. 5(b) shows the transition, which causes the observed "outer" radius of the bubble to slightly exceed the value taken at the middle of the oscillation period, which corresponds the the maximum radius as defined by theoretical cylindrical bubble dynamics. The overshoot being of a few tens of micrometers, which is still below the measurement uncertainty of 0.22 mm, it is neglected.

The bubble remains almost perfectly circular throughout its growth until the beginning of its collapse, as seen in the third frame of Fig. 6(a), where the interface transitions from being bent outwards to inwards. During the bubble's collapse phase, the distance between the "inner" and "outer" radius reduces. A dark grey halo can be observed around the bubble boundary in the fifth frame. This is likely due to the friction against the Plexiglas plate where traces of non-condensable gas are mixed with the surrounding fluid. The bubble interface is slightly perturbed by remnants of broken wire. However their influence on the overall bubble dynamics is considered negligible, as it is not apparent during the first collapse and chaotic rebound phases that follow after the seventh frame. This can also be verified by comparing data in water to theory. The cavitation bubbles in Figs. 6(b)-(e) have been generated in the shear-thickening cornstarch suspensions. In these images, only the "outer" radius is apparent, which has been verified by comparing values between water and a low volume fraction cornstarch suspension with frontlight illumination. The bubbles appear dark against the light background of the more reflective cornstarch mixture.

The presence of cornstarch particles burnt by the spark during bubble expansion and pushed against the Plexiglas wall and bubble boundary also contribute to darkening the cavity and are visible after collapse. Up to $\phi = 0.37$, the small amount of darker particles remains dispersed and is only mixed with the fluid during collapse and scattered by the flow inversion during the rebound, as shown in Fig. 6(b). However, for cornstarch suspensions with higher volume fractions, such as those in Figs. 6(c)-6(e), the particles aggregate in a thin, yet compact layer of burnt cornstarch that remains adjacent (but not adhered) to the Plexiglas wall after collapse. This phenomenon has become the main challenge of this study, as it obstructs vision of the collapse in higher solids fraction suspensions.

In Fig. 6 (see also the corresponding videos in supplemental material [56]), one sees broken pieces of wire of radius smaller than 150 μm as bright spots ejected from the bubble center. They are considered to have no noticeable effect on the bubble dynamics and act as markers that can be seen under the layer of burnt cornstarch and, when visible in subsequent frames, they provide information on the direction of the flow.

The bubbles generally keep their cylindrical shape up

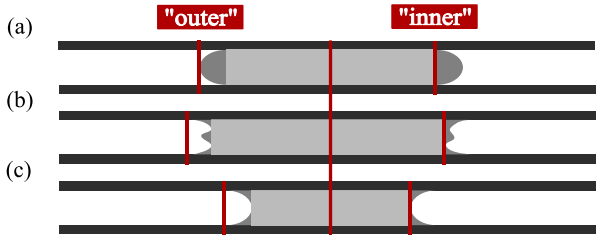

FIG. 5. Side view of a cylindrical cavitation bubble at (a) the moment it reaches its maximum volume, while displaying its shape adopted during expansion, (b) the moment the bubble interface transition from its expansion shape to its collapse shape, (c) the moment it collapses showing its collapse shape. The "outer" and "inner radii are displayed on the left and right side of the bubble, respectively. The "outer" radius in (b) slightly overshoots the one in (a) due to the transition in interface shape.

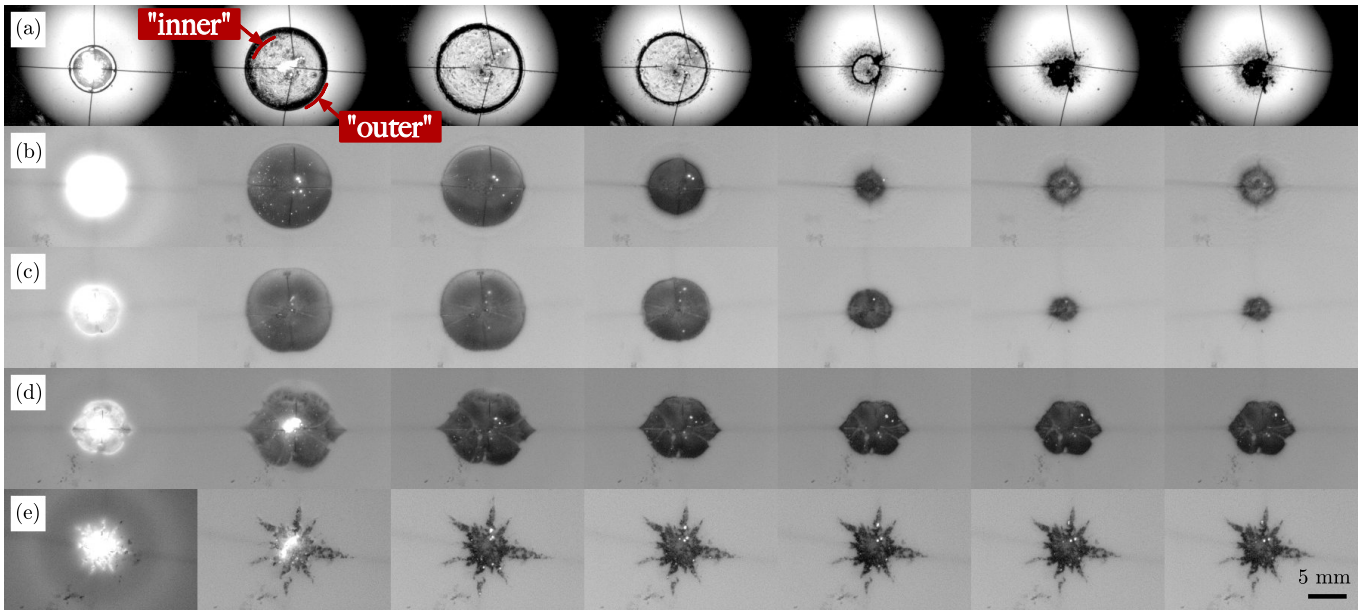

FIG. 6. Selected frames from 125 kFPS visualizations of nominally cylindrical spark-induced bubbles in (a) water, and in cornstarch suspensions of volume fractions (b) $\phi = 0.37$, (c) $\phi = 0.44$, (d) $\phi = 0.46$ and (e) $\phi = 0.52$. Every sequence shows instants $t = 0.32$, 0.80, 1.28, 1.60, 1.92, 2.24 and 2.32 ms, with $t = 0$ ms defined as spark ignition. The brightness of all frames has been increased.

to $\phi = 0.44$, which is the volume fraction limit beyond which the transition from CST to DST of the fluid behavior is expected to occur. The bubbles become clearly deformed in the suspension with $\phi = 0.46$, and two spikes following the horizontal electrode-wire are observed. Finally at $\phi = 0.52$, above which success rate of spark ignition drops drastically, no more bubble dynamics can be observed. Rather, the fluid behaves like a solid and fractures appear. The fracture branches visible in such experiments are long compared to their width, and typically 6 to 11 branches are observed. However, one cannot exclude the possible existence of invisible branches that are too small to be detected or have not breached to the surface against the transparent plate.

These results can be compared to those reported previously in Hele-Shaw cells [24, 57]. However, one must keep in mind that they are built on Stokes flow theory assuming that inertial forces are negligible compared to viscous forces, and is not valid in the present study. This is confirmed numerically by computing the Reynolds, Re, and Capillary, Ca, numbers corresponding to the simulations in Fig. 7(b)-(e), as recording the bubble wall speed is hindered during the collapse by the presence of burnt cornstarch. Their maximum values are presented in Table I. Also, viscous fingering, reported in past studies, is never witnessed in our experiments, confirming that the inertial forces are dominant during cavitation events. However, the loss of radial symmetry in Fig. 6(d) shows that the viscous forces start to counteract the inertial forces before producing actual fracture, where , $Re \approx O(10^1)$.

The fracture patterns observed here are also wider than reported in the previous studies, which induced the fracture by injection of pressurized gas. For example, [24] observed a similar number of branches as seen in the present study. However, in the gas injection inducing fractures, the branches could also bifurcate as they grew and propagated further away from the center of the applied pressure. Bifurcation of the branches was never observed with the cavitation-induced fracture. Further analysis on the fracturing phenomena is provided in section IV B 3.

TABLE I. Maximum Reynolds and Capillary numbers resulting from the numerical simulations of the four main volume fractions, as seen in Fig. 7(b)-(e).

ϕ	0.00	0.37	0.44	0.46
Re	3×10^5	5×10^2	7×10^1	1×10^1
Ca	9×10^3	2×10^3	3×10^2	6×10^0

2. *Comparison with theory*

Figure 7(a) compares the measured radius-time curves at various solids fractions corresponding to the bubbles shown in Fig. 6. The radii have been normalized to their maximum "outer" radius, and the times to the simulated collapse time of a bubble of similar maximum radius in water, $T_{\mathrm{osc,water}}$. Note that to obtain a bubble of comparable size as in lower volume fractions ($R_{\max}$ ranges between 6.45–6.75 mm for $\phi = 0.44$–0.37) the capacitor voltage (hence total discharged energy) had to be increased from 70V to 80V for the $\phi = 0.46$ mixture

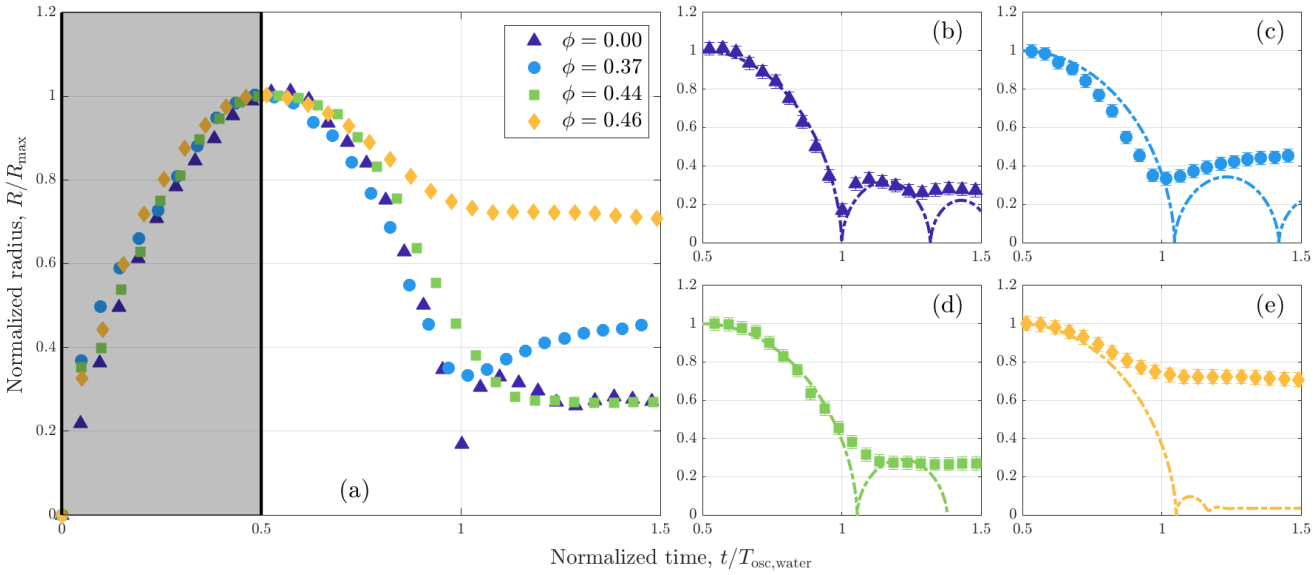

FIG. 7. (a) Normalized radius-time curves of cylindrical cavitation bubbles in water and cornstarch suspensions of increasing volume fraction, ϕ, visible in Fig. 6. The grey region depicts the growth phase. $R_{\max}$ ranges between 6.2–6.75 mm. The experimental data are compared to the Keller-Miksis equation, where the viscous term is modeled by a Cross model for (b) water, and (c) $\phi = 0.37$, (d) $\phi = 0.44$, (e) $\phi = 0.46$, cornstarch suspensions. The density and speed of sound are set accordingly to each fluid's volume fraction based on data by [26]. The errorbars show the normalized measurement uncertainty of 0.22 mm, and to improve readability, only one recorded data point in twelve is shown.

($R_{\max} = 6.2$ mm) in order to compensate for the shear-thickening effects. The oscillation period in the $\phi = 0.37$ cornstarch suspension is similar to the one in water. During the growth phase (gray-shaded region), the extracted bubble radius is overestimated due to the brightness of the spark, but this phase is in any case not considered in our analysis. The radii measured in the $\phi = 0.44$ and $\phi = 0.46$ cornstarch suspensions are highly affected by the presence of burnt cornstarch which obscured the true radius during the later half of collapse. Nonetheless, while the minimum radius was not observable in these cases, the data show the oscillation period through stabilization and a small rebound. Overall, the experiments agree with the theory quite well in the early collapse stage, but comparison of the collapse and potential rebound to the Keller-Miksis equation is limited. Despite the limitations of the experiment, it is clear that the bubble's oscillation period is longer in mixtures than in water, which is in agreement with the simulations.

In Fig. 7(b)-(e), the Keller-Miksis equation is compared with the experimental collapse and rebound phases. For bubbles in water, the measurement and theory are in satisfactory agreement up to the end of the first oscillation, beyond which the bubble loses its cylindrical shape and is strongly affected by the gap boundaries.

As the solid volume fraction increases, the agreement with theory deteriorates, and instead for $\phi = 0.37$ the theory predicts a longer collapse time compared to the experiments. Uncertainty on the exact instant of the start of the bubble collapse may have contributed to this mismatch, as the bubbles in cornstarch usually stay in the range of the maximum radius, given the experimental uncertainty, for about 20% of the oscillation time. It could also be that the recorded "outer" radius during collapse is underestimated due to opaqueness of the medium. The simulated rebound is, however, predicted to be larger than that in water due to the higher speed of sound in this mixture while being only weakly damped by viscosity.

Figure 8 shows the duration of the first oscillation period, T_{osc}, for various bubble sizes in water and cornstarch suspensions of different volume fractions. Clearly for suspensions exceeding $\phi = 0.37$ the oscillation time increases compared to water. The increased viscosity is not the only factor causing such prolongation, but also the increase in density of the mixture, while the speed of sound's contributions are minor in the first bubble oscillation. This explains why the Cross model parameter values shown in Fig. 2, when used in the numerical simulations of Fig. 4, suggest shorter collapse times than the experiments for $\phi = 0.44$ and $\phi = 0.46$. The shaded region of Fig. 8 depicts the oscillation periods simulated through the Keller-Miksis equation and bounded by water and a $\phi = 0.46$ cornstarch suspension (lower and upper lines, respectively). In order to be comparable to the oscillation period, the collapse time T_{c} is doubled assuming symmetrical growth and collapse. All measured oscillation times for $\phi = 0.46$ exceed the simulated pre-

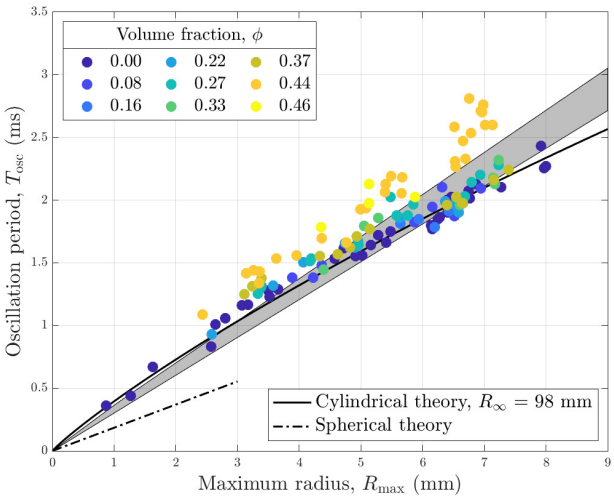

FIG. 8. The measured oscillation period of spark-induced cylindrical cavitation bubbles in water and cornstarch suspension of different volume fraction, ϕ, for different maximum radii (corresponding to varying spark energies). Curves show the cylindrical [Eq. (3)] and spherical Rayleigh collapse time equations, doubled to be comparable to T_{osc}. The highlighted region shows the numerically simulated boundaries of the oscillation period using the Keller-Miksis equation for cornstarch suspensions of $\phi = 0.00$ and $\phi = 0.46$. Note: The uncertainty in T_{osc} is smaller than the marker, while the uncertainty on R_{max} is estimated to 0.22 mm and is not shown to improve readability.

dictions, which gives a reason to question the validity of the rheometry measurements and of the Cross model at very high shear rates, or the definition of the experimental oscillation period. Indeed, as noted previously when the shear is increased, a shear-thinning phase may follow shear thickening, which would not be well represented by the Cross model. Additionally, friction with the Plexiglass plates possibly increased by presence of burned cornstarch particles in contact with the Plexiglas plates may be delaying the collapse. Note that although slippage of the shear-thickening mixtures against the parallel plates [58] has not been clearly distinguished from the bubble dynamics, its influence can currently not be excluded.

One also notices that the Keller-Miksis integration expects a linear relationship between maximum radius and oscillation period, as for spherical bubbles. However, the oscillation period based on the cylindrical Rayleigh collapse time, T_c, as expressed in Eq. (3) and shown by the solid line in Fig. 8, has a better agreement with the measurements. As this incompressible equation does not account for viscosity, it is only fitted to data of cavitation in water and the fit to the measurements yields a R_∞. This fitted value is within 2% of R_{cell}, which might be telling on the effects of confinement on bubble dynamics. However, the confinement effect has not been investigated further in the scope of this research.

The Rayleigh collapse time equation for spherical bubbles has also been plotted in Fig. 8 (dash-dotted line). One might expect the bubbles near 1-mm radius to be closer to it, since $R_{max} = 1$ mm is the limit for a spherical bubble to exist within the 2-mm gap. This, however, is not the case for the few tests that were conclusive in this range, which could be explained by the prolongation of the oscillation time due to the proximity of solid boundaries [59]. Note that reflection of spark-induced shock waves against the test-cell boundaries are considered to have a negligible effect on bubble dynamics. This is due to the fact that cylindrical propagation attenuates the pressure wave's peak pressure over the travelled distance, which is approximately 18 cm in order to come back to the bubble interface during experiments [60]. The interaction with the two parallel plates induces further reflection, leading to interaction between reflected shocks, which contribute to weakening the overall pressure transient. Furthermore, granular suspensions have proven to be efficient means for shock wave attenuation, due to their interaction with solid particles [61].

3. *Fracture patterns*

Fig. 6(e) shows cavitation-induced fracture in a $\phi = 0.52$ volume fraction cornstarch suspension, where rapidly growing dynamic jamming fronts are created by cornstarch particles interaction in the fluid [4]. It is henceforth referred to as a fracture pattern with branches, as no bubble dynamics are exhibited in this case. In contrast to the finite expansion time of a cavitation bubble, the event of fracturing occurs in the first instants of the process, while the spark continues to deposit energy into the system.

A better view on the fracturing is shown in Fig. 9, where the illumination has been lowered during the spark's presence in order to avoid saturation that would hide the actual fracture branches. Figures 10(a)-(c) show different fracture patterns visible at the discontinuation instant of the spark. This corresponds to the maximum size of the pattern before the relaxation of the fluid, which results in a partial "healing" of the fractures. This final event only lasts a few milliseconds, which is in the same order of magnitude as the relaxation time, k found in Fig. 2 for $\phi = 0.52$. Higher spark voltages result in a larger fracture patterns, which, however, remain consistent in shape.

Figure 10 shows fracture quantities extracted from the visualizations in a $\phi = 0.52$ volume fraction cornstarch suspension where the input energy is varied through the spark voltage. Results may be compared to literature where similar fractures are observed as a consequence of injecting pressurized gas into a cornstarch suspension [24]. To enable a comparison, the initial pressure generated by the spark, $p_i = p_v(T_\infty) + p_{g,0}$, where the vapor term is assumed constant and negligible, is estimated by finding the initial partial pres-

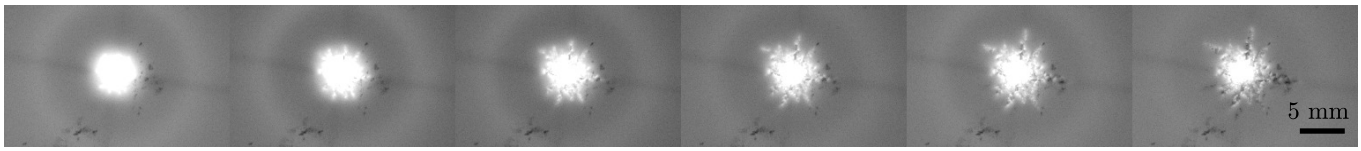

FIG. 9. Time series of the cavitation-induced fracture in a cornstarch suspension of $\phi = 0.52$. The interframe time is 80 μs with the first frame occurring 160 μs after spark ignition.

sure of the non-condensable gas, $p_{g,0}$, necessary for the Keller-Miksis equation to reach the mean maximum radius of all tests conducted at a specific capacitor voltage in water. As initial conditions, the computation uses $R_0 = 0.15$ mm estimated as the initial radius of the plasma generated by the wire-electrodes of this same diameter, and $\dot{R}_0 = 0$ m/s. The resulting initial pressures range between 100–500 bar with capacitor voltages ranging between 60–90 V (corresponding to discharge energies of $E = \int u(t)i(t)\mathrm{d}t \approx U^2C = 11.9$–$26.7$ J) and are displayed as a color scale in Fig. 10. The pressures encountered in this research are 1 to 2 orders of magnitude higher than in literature, however the energy input from simple pressure times volume change estimate in [24] is of the same order of magnitude up to ≈ 6 J.

The fracture speed is deduced by recording the time it takes for the first fracture branch to reach a circle of 4-mm radius, centered on the point where the spark ignites. By choosing such an arbitrary value, one expects higher speeds for higher input energies, as the fracture pattern is bigger. Yet in general, the data in Fig. 10 show that the fracture speed in such a cornstarch suspension range between, v =10–20 m/s, which is in the same order of magnitude as reported in literature, using a similar approach [24]. This last point interestingly suggests that although initial pressures are estimated to be much higher, the fracture speed seems to converge to a maximum value. Also note that the mean fracture speed is comparable to the mean expansion speed of cavitation bubbles in water from ignition to reaching a 4-mm radius.

Finally, the aspect ratio, A, is a dimensionless parameter quantifying the ratio of the mean spacing between branches to the maximum radius of the circular area shown in Fig. 10(d), computed as

$$A = \frac{2\pi R_{\max} - P_{\mathrm{dark}}}{2\pi R_{\max} N_{\mathrm{branch}}}, \tag{6}$$

where $R_{\max}$ is deduced from the area of the fracture pattern as an equivalent radius at the discontinuation instant of the spark, P_{dark} is the circular perimeter passing over dark fracture branches computed by counting the number of dark pixels on a 1-pixel-wide ring of inner radius $R_{\max}$, and N_{branch} is the number of branches having reached $R_{\max}$. This number gives indication on the shape of the fractures: close to zero, the branches are very thick and short while close to 1, they are very thin and long. As could be expected for tests conducted in a similar cornstarch suspension, the aspect ratio stays constant through out the test with a mean value of 0.1 $\pm$ 0.02, as shown in Fig. 10. In most of the tests, slightly larger fractures are visible along the wire-electrodes shown in black in Fig. 10(a), which suggests the wires to act as a weakness favorable for propagation. Also note that fracture patterns in the present study are relatively wide compared to [24], where the reported fractures were slim and typical for brittle materials.

V. CONCLUSIONS

A theoretical and experimental investigation of cavitation in a shear-thickening fluid is presented for the first time. The theoretical simulations are based on the

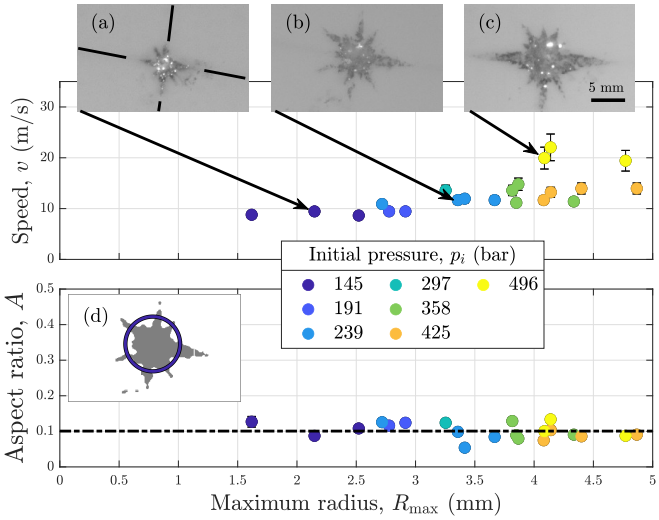

FIG. 10. Mean fracture speed (top) and aspect ratio (bottom) of cavitation-induced fracture in a shear-thickening fluid (cornstarch suspension of $\phi = 0.52$) for different maximum radii $R_{\max}$. The color of the symbols indicates the estimated initial gas pressure generated by the spark, and the dash-dotted line shows the mean value for the aspect ratio. Images of different fracture patterns for a capacitor charged at (a) 60 V and showing the wire-electrodes, (b) 70 V, and (c) 90 V, are visible, as well as (d) image showing the equivalent circular area computed from the dark pixels of the fracture shape in image (b). The circle shows the maximum radius, $R_{\max}$. The uncertainty on v and A are indicated by error bars sometimes hidden by their marker. They are computed from a 95% confidence interval Monte Carlo simulation, using the usual 0.22 mm inaccuracy on distances such as $R_{\max}$ and P_{dark} and 40 μs on time.

relatively simple Keller-Miksis-Cross model adapted to shear-thickening fluids and reveal the properties expected from such a fluid to show actual shear-thickening viscous effects, distinguishable from an inviscid or Newtonian viscous fluid. A minimum infinite shear viscosity of 3×10^{-2} Pa s is necessary to start distinguishing the collapse time from the inviscid one. Up to an infinite shear viscosity of 4 Pa s, the collapse time only increases to 10% of the inviscid collapse time. However, the relaxation time drastically increases this value when reduced below 10^{-3} s. The simulations also reveal damped dynamics and higher collapse times for increasing fluid viscosity. Overall, although the Cross model fits the rheometry data reasonably well, better models might be deduced by probing higher shear rates.

From the experiments, the bubble oscillation period could be measured and compared to that predicted from theory. Only for solids fraction above $\phi = 0.37$ does the oscillation period begin to noticeably deviate from theory in water, although this is more likely due to increased shear viscosity and density of the particle suspensions rather than their shear-thickening nature. Shear-thickening effects on the observed bubble shapes appear to become important only in the discontinuous shear thickening regime, starting from $\phi = 0.37$, where the bubbles are increasingly distorted and eventually show cavitation-induced fracture starting at solids fractions between $\phi = 0.37$ and $\phi = 0.52$. This behavior is similar to recently reported fracturing in a shear-thickening fluid by a sudden introduction of compressed gas [24], where fracture propagation speeds are between 10-20 m/s.

The observed discrepancy of the oscillation periods between experiments and theory might be caused by unaccounted wall effects in the cylindrical cavitation bubble dynamics equations. The uncertainty associated with the extrapolation of the rheometry data to constant infinite shear viscosity may also contribute to the discrepancy, making the Cross model invalid for this purpose. For similar cornstarch water suspensions, utilizing different rheometer techniques, very non-Cross like shear-thinning, thickening and thinning again behaviour as a function of monotonically increasing shear rate has been reported [25, 36]. Presently, rheometers capable of covering shear rates up to 10^6, way higher than for commercially available rheometry approaches, have been reported [62, 63], which might help in overcoming the uncertainty related to high shear rate rheometry. However, as they often rely on very small gaps in parallel plate geometries, they will be limited by the particle sizes in suspensions and this is where cavitation rheology may offer a useful additional method for characterizing such complex fluids. Study of the viscosity of opaque shear-thickening fluids could be achieved by improving current theoretical models for cylindrical cavitation bubble dynamics, and improving the experimental setup used in this study. The use of a shorter spark duration and increase of voltage, or use of a laser in optically transparent fluids to mitigate burning of the particles could potentially reduce the measurement uncertainty.

Further study could benefit from tests in a clear particle suspension such as fumed silica particles in Polyethylene Glycole [64]. This would improve the extraction of quantities such as the time at which the bubble radius extracted from experiments diverges from theory, which appears to happen earlier with increasing ϕ. In general, a wider variety of particle suspensions could be examined to enable observing more significant differences between shear-thickening and Newtonian viscous effects on the oscillation period.

ACKNOWLEDGEMENTS

G.T. Bokman and O. Supponen thank Prof. Dr. Mark Tibbitt for lending his rheometer. S.A. Mäkiharju gratefully acknowledges the support of UC Berkeley's Powley fund for the seed funding that helped start this project.

[1] E. D. Wetzel, Y. Lee, R. G. Egres, K. M. Kirkwood, J. E. Kirkwood, and N. J. Wagner, in *AIP conferr. proc.*, Vol. 712 (Am. Inst. Phys., 2004) pp. 288–293.
[2] J. Qin, B. Guo, L. Zhang, T. Wang, G. Zhang, and X. Shi, Composites Part B **183**, 1 (2020).
[3] A. Srivastava, A. Majumdar, and B. S. Butola, Crit. Rev. Solid State Mater. Sci. **37**, 115 (2012).
[4] E. Brown and H. M. Jaeger, Rep. Prog. Phys. **77**, 1 (2014).
[5] T. C. De Goede, K. G. De Bruin, and D. Bonn, Sci. Rep. **9**, 1 (2019).
[6] C. A. Brennen, *Cavitation and bubble dynamics* (Camb. Univ. Press, 2014).
[7] E.-A. Brujan, Europhys. Lett. **50**, 175–181 (2000).
[8] E.-A. Brujan and P. R. Williams, Rheol. Rev. , 147 (2005).
[9] E.-A. Brujan, *Cavitation in non-Newtonian Fluids* (Springer, 2011).
[10] M. Jalaal, M. K. Schaarsberg, C.-W. Visser, and D. Lohse, J. fluid Mech. **880**, 497 (2019).
[11] E. Turkoz, A. Perazzo, H. Kim, H. A. Stone, and C. B. Arnold, Phys. Rev. Lett. **120**, 1 (2018).
[12] J. Jiménez-Fernández and A. Crespo, Ultrasonics **43**, 643 (2005).
[13] W.-J. Yang and M.-L. Lawson, J. App. Phys. **45**, 754 (1974).
[14] R. W. Time and A. H. Rabenjafimanantsoa (2011).
[15] L. Zhang, C. Yang, and Z.-S. Mao, J. Non-Newtonian Fluid Mech. **165**, 555 (2010).
[16] D. B. Khismatullin and A. Nadim, Phys. Fluids **14**, 3534 (2002).
[17] A. A. Doinkov and P. A. Dayton, J. Acoust. Soc. **121**, 3331 (2007).

[18] B. Dollet, P. Marmottant, and V. Garbin, Annu. Rev. Fluid Mech. **51**, 331 (2019).

[19] C. W. Barney, C. E. Dougan, K. R. McLeod, A. Kazemi-Moridani, Y. Zheng, Z. Ye, S. Tiwari, I. Sacligil, R. A. Riggleman, S. Cai, J.-H. Lee, S. R. Peyton, G. N. Tew, and A. J. Crosby, Proc. Natl. Acad. Sci. **117**, 9157 (2020).

[20] J. B. Estrada, C. Barajas, D. L. Henann, E. Johnsen, and C. Franck, J. Mech. Phys. Solids **112**, 291 (2018).

[21] J. A. Zimberlin and A. J. Crosby, J. Polym. Sci. **48**, 1423 (2009).

[22] P. Cui, Q. X. Wang, S. P. Wang, and A. M. Zhang, Phys. Fluids **28**, 1 (2016).

[23] O. Supponen, D. Obreschkow, P. Kobel, N. Dorsaz, and M. Farhat, Exp. Fluids **60**, 1 (2019).

[24] D. Ozturk, M. L. Morgan, and B. Sandnes, Comm. Phys. **3**, 1 (2020).

[25] A. Fall, F. Bertrand, D. Hautemayou, C. Mezière, P. Moucheront, A. Lemaître, and G. Ovarlez, Phys. Rev. Lett. **114**, 1 (2015).

[26] E. Han, N. Van Ha, and H. M. Jaeger, Soft Matter **13**, 3506 (2017).

[27] N. C. Crawford, L. B. Popp, K. E. Johns, L. M. Caire, B. N. Peterson, and M. W. Liberatore, J. Colloid Interface Sci. **396**, 83 (2013).

[28] C. Chevalier, A. Lindner, M. Leroux, and E. Clement, J. Non-Newtonian Fluid Mech. **158**, 63 (2009).

[29] K. Yasui, *Acoustic Cavitation and Bubble Dynamics* (Springer, 2018).

[30] S. Von Kann, J. H. Snoeijer, D. Lohse, and D. Van Der Meer, Phys. Rev. E **84**, 1 (2011).

[31] B. M. Borkent, M. Arora, C.-D. Ohl, N. De Jong, M. Versluis, D. Lohse, K. A. Mørch, E. Klaseboer, and K. B. Cheong, J. Fluid Mech. **610**, 157 (2008).

[32] L. Sair and W. R. Fetzer, J. Non-Newtonian Fluids Mech. **36**, 205 (1944).

[33] I. R. Peters, S. Majumdar, and H. M. Jaeger, Nature **532**, 214 (2016).

[34] A. Fall, F. Bertrand, and G. Ovarlez, J. Rheol. **56**, 575 (2012).

[35] M. M. Cross, J. Colloid Sci. **20**, 417 (1965).

[36] F. Galindo-Rosales, F. J. Rubio-Hernández, A. Sevilla, and R. Ewoldt, J Non-Newtonian Fluid Mech. **166**, 1421 (2011).

[37] N. J. Wagner and J. F. Brady, Phys. Today **62**, 27 (2009).

[38] F. T. Trouton, Proc. Roy. Soc. A **77**, 426 (1906).

[39] O. Cheal and C. Ness, J. Rheol. **62**, 501 (2018).

[40] M. M. Denn, J. F. Morris, and D. Bonn, Soft Matter **14**, 170 (2018).

[41] M. Roché, H. Kellay, and H. A. Stone, Phys. Rev. Lett. **107**, 1 (2011).

[42] E. E. B. White, M. Chellamuthu, and J. P. Rothstein, Rheol. Acta. **49**, 119 (2010).

[43] M. Guémas, A. G. Marìn, and D. Lohse, Soft Matter **8**, 10725 (2012).

[44] P. A. Quinto-Su, K. Y. Lim, and C.-D. Ohl, Phys. Rev. E **80**, 1 (2009).

[45] S. R. Gonzalez-Avila, E. Klaseboer, B. C. Khoo, and C.-D. Ohl, J. Fluid Mech. **682**, 241 (2011).

[46] E. Zwaan, S. Le Gac, K. Tsuji, and C.-D. Ohl, Phys. Rev. Lett. **98**, 1 (2007).

[47] G. L. Chahine and P. F. Genoux, J. Fluids Eng. **105**, 400 (1983).

[48] L. Rayleigh, Philos. Mag. **34**, 94 (1917).

[49] F. R. Gilmore (1952).

[50] J. B. Keller and M. Miksis, J. Acoust. Soc. Am. **68**, 628 (1980).

[51] M. S. Plesset, ASME. J. Appl. Mech. **16**, 277 (1949).

[52] Y. A. Ilinskii, E. A. Zabolotskaya, T. A. Hay, and M. F. Hamilton, J. Acoust. Soc. Am. **132**, 1346 (2012).

[53] D. Jasikova, P. Schovanec, M. Kotek, and V. Kopecky, EPJ Web Conf. **180**, 1 (2018).

[54] M. Favelukis and R. J. Albalak, The Chem. Eng. J **63**, 149 (1996).

[55] W.-J. Yang and H.-C. Yeh, AIChE J. **12**, 927 (1966).

[56] G. T. Bokman, O. Supponen, and S. A. Mäkiharju, See supplemental material at [url will be inserted by publisher] for videos showing cavitation bubbles in fig. 6. all files related to a published paper are stored as a single deposit and assigned a supplemental material url. this url appears in the article's reference list. (2021).

[57] L. Kondic, M. J. Shelley, and P. Palffy-Muhoray, Phys. Rev. Lett. **80**, 1433 (1998).

[58] B. Saint-Michel, T. Gibaud, and S. Manneville, Phys. Rev. X **8**, 1 (2018).

[59] P. Gregorčič, R. Petkovšek, and J. Možina, J. Appl. Phys. **102**, 1 (2007).

[60] Q. Liu and Y. Zhang, J. App. Phys. **116**, 153302 (2014).

[61] S. Medvedev, S. Frolov, and B. Gel'fand, J. Eng. Phys. Thermophys. **58**, 714– (1990).

[62] K. S. Mriziq, H. J. Dai, M. D. Dadmun, G. E. Jellison, and H. D. Cochran, Rev. of Sci. Instruments **75**, 2171 (2004).

[63] C. J. Pipe, T. S. Majmudar, and G. H. McKinley, Rheol. Acta. **47**, 621 (2008).

[64] M. Singh, S. K. Verma, I. Biswas, and R. Mehta, J. Fluid Mech. **39**, 48 (2019).